Manipulider: A Multi-Engine Buoyancy-Controlled Robot for Thrusterless Underwater Gliding and Manipulation

Hidden

***Abstract*—The MANIPULIDER is a buoyancy-actuated underwater robot that enables thrusterless, glide-like locomotion and attitude-based manipulation, while providing a magnetic modular interface for rapid payload swapping (e.g., a gripper or sensors). Four syringe-based buoyancy engines distributed around the body jointly regulate net buoyancy and the center of buoyancy, allowing the vehicle to maintain large tilt angles through static force balance without continuous thrust and to avoid propeller entanglement risks. We present the mechanical and electrical design, calibration procedure, and control architecture. Experiments with a gripper attached (no external payload) show a controllable buoyancy-displacement range of 40 mL per engine (≈160 g total buoyancy authority), maximum statically stable tilts of 64.6° (single-engine) and 61.8° (dual-engine), and representative vertical and tilt-transition dynamics. We further demonstrate tilt regulation, controlled ascent/descent primitives, and a thrusterless manipulation sequence transporting a grasped payload.**

***Index Terms*—Underwater robotics, buoyancy control, attitude control, thrusterless locomotion, underwater gliding, modular payload platform**

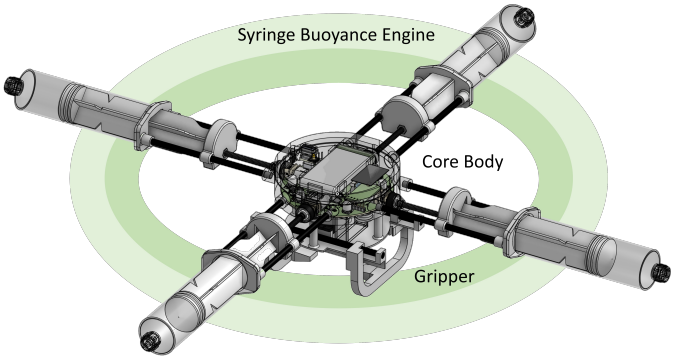

Fig. 1. System overview of MANIPULIDER (CAD rendering). The robot consists of a sealed central body with four syringe-based buoyancy engines arranged symmetrically around the frame, and a magnetically attached gripper module mounted underneath. The multi-engine layout enables both net buoyancy modulation and differential buoyancy distribution for posture control.

I. INTRODUCTION

Underwater robots are increasingly deployed for inspection, monitoring, and intervention tasks in complex natural environments. However, long-duration operation and reliable mobility remain challenging due to energy constraints and the difficulty of maintaining stable posture in the presence of currents and obstacles [1]–[3].

Most autonomous underwater vehicles (AUVs) use thrusters (and sometimes control surfaces, such as fins) to regulate depth and attitude. Thruster-driven platforms can be highly maneuverable, but are inherently power-inefficient and can produce significant disturbance and noise [4], because they need continuous actuation to maintain a particular attitude. In cluttered environments, propellers may also be susceptible to interference or entanglement, which can compromise reliability [5]. These limitations motivate alternative actuation strategies that can maintain posture with low steady-state power.

Buoyancy-driven systems offer an appealing direction because they can change depth by regulating displaced volume, enabling efficient long-range motion in the style of underwater gliders [6], [7]. Recent work has also explored compact and soft implementations, including fluidic closed-loop control for untethered gliders [8]. Nevertheless, many buoyancy-driven robots achieve limited volume change relative to vehicle size and therefore have limited buoyancy authority, which constrains payload capacity and the range of achievable operating conditions. In addition, attitude control is often realized by shifting the center of mass (e.g., translating an internal battery), which can provide only a limited posture range and controllability [9]–[12]. As a result, many platforms still rely on thrusters or auxiliary mechanisms to achieve agile posture changes or to robustly manage ascent and descent.

This paper presents MANIPULIDER (Fig. 1), a buoyancy-actuated underwater robot that combines thrusterless, glide-like locomotion with attitude-based manipulation and modular payload integration. Four buoyancy engines distributed around the body jointly regulate net buoyancy and the buoyancy center, enabling statically stable, whole-body tilting without continuous thrust. A magnetic payload interface mounted underneath supports rapid swapping of task-specific modules (e.g., a gripper or sensors). Experiments show that the platform can hold large tilt angles in water (up to 64.6° in a single-engine configuration with a gripper attached).

At the mechanism level, MANIPULIDER adopts a multi-engine variable-buoyancy architecture based on syringe-type volume change. Compared with a single large variable-volume chamber, distributing buoyancy actuation across multiple smaller engines reduces the pressure-loaded area per actuator, thereby lowering the required actuation force at depth and relaxing material strength requirements. Moreover, buoyancy margin and payload capability can be increased by adding engines, offering a scalable design path.

Manuscript 2663 submitted to 2026 IEEE/RSJ International Conference on Intelligent Robots and Systems (IROS). Received March 3, 2026.

The main contributions of this work are:

- A multi-engine buoyancy-controlled underwater robot that jointly regulates net buoyancy and the buoyancy center for wide-range, statically stable whole-body tilting.
- A control architecture for stable hovering at multiple attitudes and thrusterless, glide-like translation primitives via coordinated buoyancy and posture commands.
- A magnetic modular payload interface enabling rapid integration of task-specific modules, with gripper-based manipulation demonstrations.
- An experimental characterization of the robot's performance (summarized in Table I), quantifying a usable buoyancy displacement of 10–50 mL per engine (≈160 g total authority), maximum statically stable tilts of 64.6° (single-engine) and 61.8° (dual-engine), and representative vertical/tilt transition dynamics.

TABLE I
SUMMARY OF THE MANIPULIDER PROTOTYPE CHARACTERISTICS.

Metric	Value
Base robot mass	399.2 g
Gripper module mass	86.7 g
Max statically stable tilt angle (single-engine)	64.6°
Max statically stable tilt angle (dual-engine, diagonal)	61.8°
Representative tilted-hover equilibrium tilt angle	52.8° (0.921 rad)
Peak tilt rate during transition	0.332 rad/s
Peak tilt acceleration during transition	0.528 rad/s^2
Ascent max speed	56.2 mm/s
Ascent max acceleration	362.3 mm/s^2
Descent max speed	95.5 mm/s
Descent max acceleration	370.0 mm/s^2

II. RELATED WORK

This section reviews prior work on (i) thruster-driven AUVs and buoyancy-driven gliders, (ii) variable-buoyancy mechanisms and buoyancy/balance control, (iii) attitude control via internal mass shifting versus distributed buoyancy (i.e., center-of-buoyancy manipulation), and (iv) modular payload interfaces and underwater manipulation. We emphasize how MANIPULIDER differs in actuation design and the resulting control authority, particularly for multi-attitude hovering without continuous thrust.

A. Thruster-Driven AUVs and Buoyancy-Driven Gliders

Thruster-driven AUVs provide agile maneuverability and are well-suited for operation in complex environments; however, they typically incur substantial energy consumption and can introduce non-negligible hydrodynamic disturbances. In contrast, underwater gliders achieve efficient long-range motion by cycling buoyancy and commonly rely on internal mass shifting and/or control surfaces for attitude regulation [6], [7]. Classic glider systems and models established the canonical framework in which periodic changes in buoyancy and internal mass distribution convert vertical excursions into horizontal displacement with ultra-low power consumption [9], [10], [13]–[16]. Follow-up work improved depth regulation by increasing the accuracy and repeatability of buoyancy actuation and associated sensing [17]. These foundations underscore the endurance advantage of buoyancy-driven locomotion, while also highlighting limitations in maneuverability and fine-grained posture authority, especially for small-scale platforms.

Recent efforts aim to narrow this gap by improving maneuverability while retaining the efficiency benefits of buoyancy actuation. For example, ReefGlider proposes a platform based on a vectored buoyancy engine, targeting enhanced maneuverability under buoyancy-only control [4]. MANIPULIDER shares the motivation to reduce reliance on thrusters, but focuses on distributed buoyancy engines that directly modulate the center of buoyancy to enable wide-range hovering and controlled glide transitions under a common actuation suite, while also emphasizing modular payload integration.

B. Variable Buoyancy Mechanisms and Buoyancy/Balance Control

Buoyancy control has been explored through bio-inspired mechanisms, such as the phase change of spermaceti oil in sperm whales [18]. Other designs develop compact variable-buoyancy devices for long-duration vertical profiling and low-power locomotion, including soft and fluidic actuation and closed-loop control [8], [19]. Research has also addressed buoyancy and balance regulation during dynamic payload changes Detweiler *et al.* present mechanisms and control algorithms that adapt buoyancy and balance without increasing thruster workload [20]. Related hovering platforms explore buoyancy and balance control to reduce steady thruster usage under changing payload conditions (e.g., AMOUR V) [21].

Beyond single-vehicle demonstrations, recent work increasingly frames variable-buoyancy systems (VBS) as reusable subsystems for small AUVs and gliders. Electromechanical and electrohydraulic buoyancy-change modules have been developed and experimentally evaluated, exploring trade-offs among authority, packaging, and robustness [22], [23]. A comparative study further quantified the dynamic response and power requirements of VBS versus propeller-based actuation, reinforcing the efficiency advantage of buoyancy-driven depth control for long-duration missions [24]. Additional studies examine VBS design and control for hovering and miniature implementations, informing practical design choices at small scale [25], [26]. While these efforts improve repeatable buoyancy actuation and depth regulation, many modules primarily target endurance and profiling rather than wide-range, statically stable attitude control via buoyancy distribution. Thermal energy engines offer an orthogonal route to endurance [27], but do not directly address agile attitude authority through rapid and precise buoyancy redistribution.

C. Attitude Control: Mass Shifting vs. Distributed Buoyancy

A common approach for buoyancy-driven vehicles is to shift internal masses to change the center of mass and thereby regulate pitch and roll, often in combination with buoyancy cycling and control surfaces [9], [10], [13]–[15]. While effective for many glider missions, the achievable attitude range

Manuscript 2663 submitted to 2026 IEEE/RSJ International Conference on Intelligent Robots and Systems (IROS). Received March 3, 2026.

and control bandwidth are often constrained by mechanical travel, internal packaging, and the accuracy/repeatability limits of buoyancy and depth regulation [10], [17]. In contrast, distributed buoyancy actuation directly changes the center of buoyancy (CoB), enabling buoyancy-generated restoring torques that can maintain nontrivial attitudes through static force balance. ReefGlider provides an example of enhancing control authority via buoyancy-based actuation elements [4]. MANIPULIDER contributes a compact, syringe-based multi-engine design and targets a wide range, statically stable multi-attitude hovering without continuous thrust by coordinating both net buoyancy and CoB.

D. Modularity, Magnetic Interfaces, and Underwater Manipulation

Modularity and magnetic coupling have been used in underwater robotics to improve reconfigurability while mitigating sealing challenges. For example, MMBAUV uses magnetically coupled modules to enable modular bio-inspired swimming while addressing watertightness constraints [28]. Magnetic alignment has also been explored for underwater docking to facilitate recharging or reconfiguration [29]. MANIPULIDER complements this direction by providing a magnetic payload interface intended for rapid swapping of task-specific modules beneath a common buoyancy-and-control core.

In parallel, underwater manipulation has been explored using mobile manipulation platforms and compliant arms/grippers [30], [31]. MANIPULIDER is positioned as a buoyancy-actuated platform that can potentially support such tasks by enabling multi-attitude hovering and a repeatable, rapid payload mounting interface, while maintaining thruster-less operation during hovering and gliding.

E. Summary of Differences

In summary, prior work establishes buoyancy-driven locomotion as an energy-efficient alternative to thruster-centric AUVs and explores a range of variable-buoyancy mechanisms and balance control strategies [6]–[8], [20]. MANIPULIDER differs by combining (i) distributed buoyancy engines for direct center-of-buoyancy control, (ii) wide-range, statically stable multi-attitude hovering without continuous thrust, (iii) controlled hover-to-glide behaviors through coordinated buoyancy and posture, and (iv) a magnetic modular payload interface aimed at rapid task adaptation.

III. METHODOLOGY

A. System Overview

Figure 1 gives a system-level overview of MANIPULIDER. The robot consists of a sealed central core body and four identical syringe buoyancy engines arranged symmetrically around the body. Each buoyancy engine is driven by an independent motor, enabling both net buoyancy control and differential buoyancy distribution for posture regulation. A magnetic snap interface on the underside of the body enables rapid attachment of task-specific modules (e.g., a gripper or sensors), allowing MANIPULIDER to serve as a reconfigurable

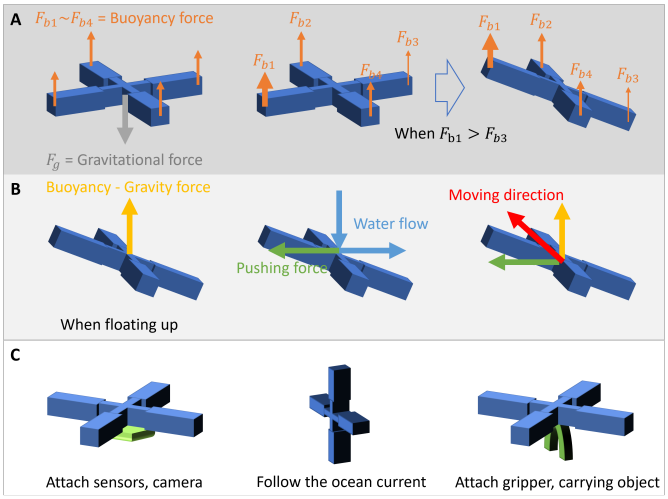

Fig. 2. Concept illustration of distributed buoyancy control. (A) Differential buoyancy across the four engines shifts the center of buoyancy and generates attitude torques. (B) Coordinating net buoyancy with a pitched attitude enables thrusterless gliding. (C) Magnetic attachment enables rapid payload changes, supporting different sensing or manipulation modules in concept.

underwater platform. The magnetic connector also provides electrical contacts for supplying power and communication to the attached payload module, enabling rapid functional reconfiguration without modifying the sealed core.

The CAD model (Fig. 1) has an overall footprint of 564.5 mm $\times$ 564.5 mm; the central body is 26 mm thick (approximately 33 mm including the top sealing port), and the gripper is 63.2 mm tall with a maximum grasp width of 61 mm.

B. Buoyancy Control Concept

We control MANIPULIDER's motion through the buoyancy forces produced by the four engines. As illustrated in Fig. 2(A), changing the relative buoyancy across the four arms shifts the center of buoyancy and produces a restoring torque that sets the robot's attitude. Unlike thruster-based attitude control, which typically requires continuous power and is vulnerable to propeller entanglement in cluttered environments [5], the proposed approach can maintain a desired attitude through static force balance with low steady-state energy consumption.

Net buoyancy controls vertical motion. When the total buoyancy exceeds the weight, the robot ascends; when it is lower, the robot descends. As shown in Fig. 2(B), if the robot holds a nonzero pitch angle while ascending or descending, hydrodynamic forces generate a horizontal component of motion, enabling thrusterless gliding. This mode can be used for energy-efficient translation without propellers. Figure 2(C) highlights the modular payload concept: by attaching different payloads beneath the body via magnets, MANIPULIDER can be adapted for a range of tasks. When equipped with a gripper, the platform can potentially support underwater manipulation tasks such as object transport and block stacking [32]–[34], which we discuss further in Sec. V.

Manuscript 2663 submitted to 2026 IEEE/RSJ International Conference on Intelligent Robots and Systems (IROS). Received March 3, 2026.

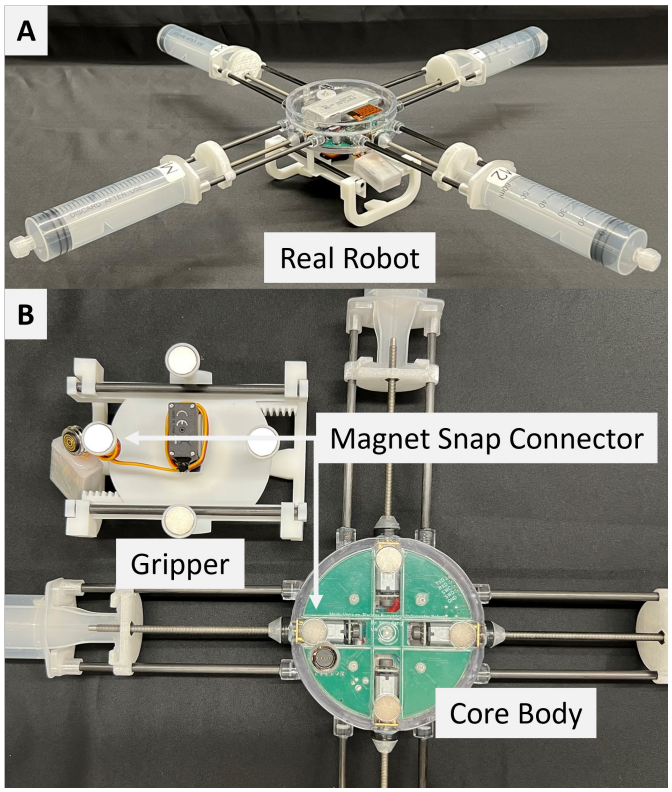

Fig. 3. MANIPULIDER prototype and magnetic snap interface. (A) Assembled robot. (B) Underside view showing the magnetic snap connector, example gripper module, and the core body.

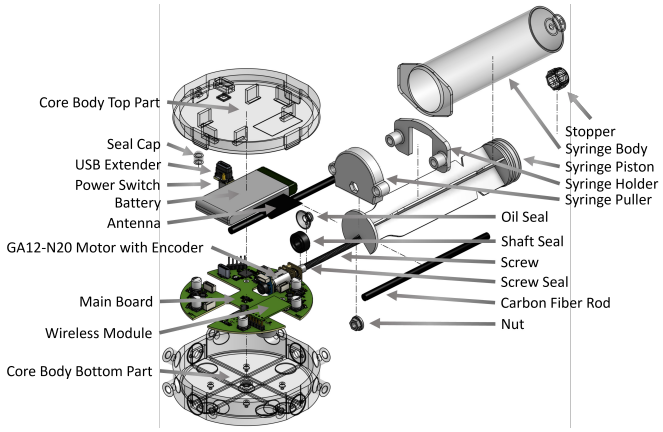

Fig. 4. Exploded assembly view of the core body and one syringe buoyancy engine, highlighting the actuation transmission and sealing components used to maintain water tightness.

C. Mechanical Design and Assembly

The physical robot is shown in Fig. 3. The central core body houses the battery, controller, motor drivers, and sensors in a sealed enclosure. The magnetic snap connector on the underside enables rapid attachment and detachment of payload modules while providing repeatable alignment. This interface is intended to support fast swapping of sensors and tools without modifying the core buoyancy-and-control platform.

Figure 4 shows an exploded view of the assembly. Each buoyancy engine is implemented using a sealed syringe (standard 60 mL graduated size) whose plunger is actuated by a motor-driven lead screw. Guide rods constrain the moving elements, reducing side loading and preventing binding during stroke. Because the system includes moving shafts and a screw transmission that operate adjacent to the wet environment, multiple seals are used along the load path (e.g., shaft seals and screw seals) to preserve water tightness while permitting motion.

We further characterize the volumetric actuation rate of each syringe engine, defined as the time derivative of displaced volume, $\dot{V}$, which directly affects the achievable buoyancy change rate $\dot{F}_b = \rho g \dot{V}$. We measure $\dot{V}$ by commanding the syringe volume (within the 60 mL graduated syringe) to sweep from 10 mL to 30 mL and recording the elapsed time; the reverse sweep (30 mL to 10 mL) is measured similarly to capture directional asymmetry due to friction and transmission effects. The measured average volume change rates are 0.98843 mL/s (10→30 mL) and 1.04801 mL/s (30→10 mL).

A key design choice is to use four identical engines rather than a single large variable-volume chamber. Distributing the pressure-loaded area across multiple smaller syringes reduces the peak force demanded from any single actuator at depth and lowers structural requirements. It also enables differential buoyancy commands for attitude control, rather than relying solely on internal mass shifting [9], [17].

The internal components are arranged as symmetrically as possible about the body center, and minor trimming mass is used during calibration to make the center of mass close to the geometric center of the vehicle. This reduces constant gravitational bias torques and improves the repeatability of buoyancy-based attitude control.

D. Electronics and Control Architecture

The electronics architecture is summarized in Fig. 5. A central controller coordinates sensing, control, and actuation. The robot uses an IMU to estimate attitude and a pressure sensor to estimate depth. Each buoyancy engine is driven by a dedicated motor with encoder feedback (hall-sensor-based), enabling closed-loop control of plunger position. The controller commands the motor driver to track target positions, enabling repeatable buoyancy changes across engines.

On the RP2040, sensing/communication and motor control are split across the two cores. Core 0 periodically acquires sensor data and services the wireless command/status link, while Core 1 runs a dedicated 1 kHz motion-control loop for the four syringe actuators. This separation prevents communication and sensor I/O latency from interfering with the timing of the actuator position control.

Power management is split into separate rails for logic and actuation. The system is built around an RP2040 microcontroller, a 6-axis IMU (3-axis accelerometer and 3-axis gyroscope), and an MS5837 pressure sensor for depth estimation. Four brushed DC motors drive the syringe plungers

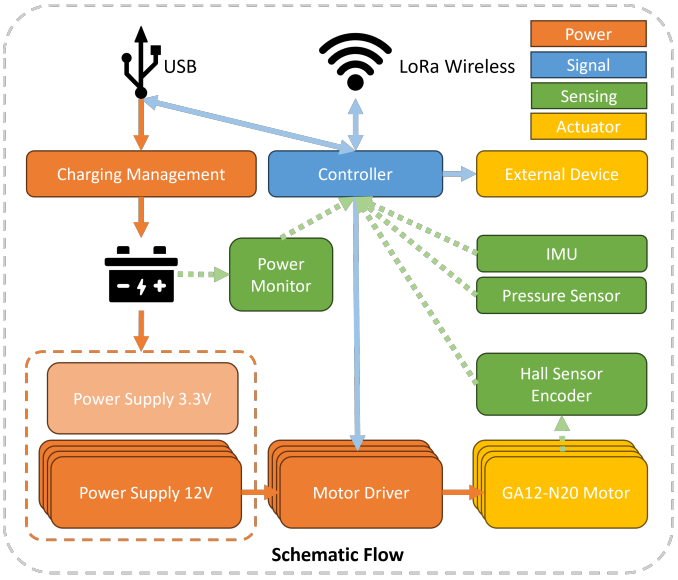

Fig. 5. Electronics architecture of MANIPULIDER. The controller reads IMU and pressure sensors for attitude and depth estimation, monitors power, and commands four motor drivers (one per buoyancy engine) using encoder feedback for closed-loop position control.

through lead screws; each motor includes a rear-mounted magnetic encoder for relative position feedback, enabling accurate closed-loop positioning of the plungers. Motor actuation is powered from a boosted 12 V rail, while logic and sensors run from a regulated 3.3 V rail. System voltage and current are monitored onboard, and a wireless UART link supports command and telemetry exchange.

E. Dynamics and Attitude Control Formulation

We define the robot pose $\boldsymbol{\eta}$ and body-fixed velocity $\boldsymbol{\nu}$ as

$$\boldsymbol{\eta} = \begin{bmatrix} \boldsymbol{p} \\ \boldsymbol{\Theta} \end{bmatrix} = \begin{bmatrix} x & y & z & \phi & \theta & \psi \end{bmatrix}^T, \tag{1}$$

$$\boldsymbol{\nu} = \begin{bmatrix} \boldsymbol{v} \\ \boldsymbol{\omega} \end{bmatrix} = \begin{bmatrix} u & v & w & p & q & r \end{bmatrix}^T, \tag{2}$$

where $\boldsymbol{p}$ is the position in the inertial frame, $\boldsymbol{\Theta}$ are roll–pitch–yaw angles, and $\boldsymbol{\nu}$ is expressed in the body-fixed frame. The rigid-body dynamics of the robot expressed in the body-fixed frame are

$$M\dot{\boldsymbol{\nu}} + \boldsymbol{C}(\boldsymbol{\nu})\boldsymbol{\nu} = \boldsymbol{\tau}, \tag{3}$$

where $M = \begin{bmatrix} mI_{3\times3} & 0 \\ 0 & I \end{bmatrix}$, m is the total mass, $I_{3\times3}$ is the 3×3 identity matrix, and I is the inertia tensor expressed in the body frame. The matrix $\boldsymbol{C}(\boldsymbol{\nu})$ denotes the rigid-body Coriolis and centripetal matrix associated with the velocity vector $\boldsymbol{\nu}$.

The total external wrench in the inertial frame is denoted by $\boldsymbol{\tau}^w$. The corresponding wrench expressed in the body-fixed frame is denoted by $\boldsymbol{\tau}$

$$\boldsymbol{\tau} = \begin{bmatrix} R^T & 0 \\ 0 & R^T \end{bmatrix} \boldsymbol{\tau}^w, \ \boldsymbol{\tau}^w = \begin{bmatrix} \boldsymbol{F}_B^w + \boldsymbol{F}_D^w \\ \boldsymbol{\tau}_B^w + \boldsymbol{\tau}_D^w \end{bmatrix}, \tag{4}$$

where $R \in SO(3)$ is the rotation matrix from body to inertial frame. $\boldsymbol{F}_B^w$ and $\boldsymbol{\tau}_B^w$ denote the buoyancy force and torque expressed in the inertial frame, while $\boldsymbol{F}_D^w$ and $\boldsymbol{\tau}_D^w$ denote the drag force and torque expressed in the inertial frame. We first define the buoyancy force and the corresponding torque generated by the four arms:

$$\boldsymbol{F}_B^w = (F_b - F_g)\boldsymbol{e}_z, \ \boldsymbol{\tau}_B^w = \sum_{i=1}^{4} (R\boldsymbol{r}_i) \times (F_{b,i}\boldsymbol{e}_z), \tag{5}$$

where $\boldsymbol{e}_z$ denotes the unit vector along the z-axis, and g denotes the gravitational acceleration. Let F_g be the gravitational force (weight) of the robot. $\boldsymbol{r}_i$ denotes the position vector of the i-th arm expressed in the body frame. We denote the buoyant force produced by engine $i \in \{1, 2, 3, 4\}$ as $F_{b,i}$. The net buoyant force is:

$$F_b = \sum_{i=1}^{4} F_{b,i}. \tag{6}$$

The sign of $\boldsymbol{F}_B^w$ determines the vertical motion regime:

- **Neutral buoyancy:** $F_b = F_g$.
- **Floating up:** $F_b > F_g$.
- **Sinking down:** $F_b < F_g$.

Since buoyancy is generated by displaced volume, a convenient intermediate variable is the displaced volume change ΔV_i of each engine, where

$$F_{b,i} = \rho g \Delta V_i, \tag{7}$$

with ρ the water density and g gravitational acceleration. In practice, ΔV_i is controlled by commanding the syringe plunger displacement, which is tracked using motor encoder feedback (Fig. 5). We calibrate an approximately linear encoder-to-volume relationship by measuring the encoder span between the syringe marks 10 mL and 30 mL. Averaged across engines, the calibration yields approximately 8138 encoder counts per mL (i.e., $\Delta n \approx 8138\,\Delta V$ with ΔV in mL), which we use to convert desired displaced-volume changes into motor position setpoints.

We then define the drag force and the corresponding torque acting on the robot:

$$\boldsymbol{F}_D^w = \sum_{i=1}^{4} \boldsymbol{F}_{D,i}, \ \boldsymbol{\tau}_D^w = \sum_{i=1}^{4} (R\boldsymbol{r}_i) \times \boldsymbol{F}_{D,i} \tag{8}$$

We denote the drag force on each arm as $\boldsymbol{F}_{D,i}$. $\boldsymbol{F}_{D,i}$ is modeled based on the component of the relative velocity perpendicular $\boldsymbol{v}_{\perp,i}$ to $\boldsymbol{r}_i$:

$$\boldsymbol{F}_{D,i} = \frac{1}{2}\rho C_D A \|\boldsymbol{v}_{\perp,i}\| \boldsymbol{v}_{\perp,i} \tag{9}$$

where ρ is the fluid density and C_D is the dimensionless drag coefficient. Define the unit vector along $\boldsymbol{r}_i$ as $\boldsymbol{a}_i = \frac{\boldsymbol{r}_i}{\|\boldsymbol{r}_i\|}$, $\boldsymbol{a}_i^w = R\boldsymbol{a}_i$. Here we assume a uniform ambient current, represented by a constant velocity vector $\boldsymbol{v}_c$ in the inertial frame. The relative velocity at the i-th arm in the inertial frame is

$$\boldsymbol{v}_{rel,i}^w = \boldsymbol{v}_c - R\boldsymbol{v}_i, \tag{10}$$

$$\boldsymbol{v}_i = \boldsymbol{v} + \boldsymbol{\omega} \times \boldsymbol{r}_i. \tag{11}$$

Manuscript 2663 submitted to 2026 IEEE/RSJ International Conference on Intelligent Robots and Systems (IROS). Received March 3, 2026.

The perpendicular component of the relative velocity is given by

$$\boldsymbol{v}_{\perp,i} = \boldsymbol{v}^{w}_{rel,i} - (\boldsymbol{v}^{w}_{rel,i} \cdot \boldsymbol{a}^{w}_{i})\boldsymbol{a}^{w}_{i}. \tag{12}$$

The formulation above supports offline computation and analysis of buoyancy-induced forces/torques during tilted ascent/descent. To maintain high-frequency control cycles on the robot's resource-constrained embedded controller, these complex calculations are not yet integrated into the real-time onboard loop; instead, high-level setpoints are tuned empirically as described below:

- A high-level depth controller (external) regulates F_b (common-mode command across the four engines) using pressure feedback.
- A high-level attitude controller (external) regulates vehicle tilt using IMU feedback through differential volume commands.
- Four low-level motor position loops track individual plunger position commands using encoder feedback.

In the current prototype, the onboard firmware provides reliable low-level execution of per-engine syringe displacement commands using motor encoder feedback, enabling repeatable volume changes and static holding. High-level setpoints (net buoyancy changes and differential commands for a desired tilt direction) are tuned empirically during experiments and may vary with payload properties and environmental conditions (e.g., trapped air, water currents, and hydrodynamic interaction). Developing a general, model-based mapping from desired depth/tilt to per-engine setpoints that remains robust across payloads and environments is an important direction for future work (Sec. V).

F. Calibration

Our current calibration procedure focuses on buoyancy trimming for stable hovering. With all four engines set to a nominal mid-stroke position, we adjust the total mass/buoyancy so that the robot reaches neutral buoyancy in still water and remains suspended. We then fine-tune the trim so that, at rest, the robot hovers with its main body approximately parallel to the ground (i.e., minimal static tilt bias).

IV. Results

Tilt angles are computed from the onboard IMU accelerometer, while speeds/accelerations are estimated from external video using a calibrated scale reference.

A. Buoyancy Performance

In vertical motion tests (gripper attached, no payload), the robot achieved a maximum ascent speed of 56.2 mm/s with a peak vertical acceleration of 362.3 mm/s^2. In descent, it reached a maximum speed of 95.5 mm/s with a peak acceleration of 370.0 mm/s^2 (Table I).

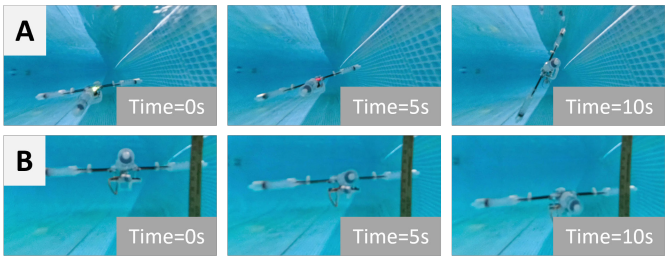

Fig. 6. Representative locomotion primitives enabled by multi-engine buoyancy control. (A) Tilt regulation: the robot changes the relative displaced volume across engines to achieve and hold a nonzero tilt angle. (B) Descent regulation: the robot decreases net buoyancy (while maintaining attitude) to perform controlled sinking without thrusters.

B. Attitude Control

To quantify the attitude authority enabled by distributed buoyancy control, we measured the maximum statically stable tilt angle in water with the gripper module attached and no external payload. For each direction, we commanded the robot to increase its tilt until it could no longer maintain a stable equilibrium. The onboard IMU accelerometer readings (a_x, a_y, a_z) were converted to a tilt angle ϑ (angle between the body z-axis and gravity) using

$$\vartheta = \arccos\left(\frac{a_z}{\sqrt{a_x^2 + a_y^2 + a_z^2}}\right). \tag{13}$$

We report the maximum statically stable tilt across single-engine and dual-engine "engine-up" configurations. Across the four single-engine cases (M1–M4, corresponding to $\pm Y$ and $\pm X$ directions), the maximum statically stable tilt reached $64.6°$. Across the four dual-engine diagonal cases (M1+M2, M2+M3, M3+M4, M4+M1), the maximum statically stable tilt reached $61.8°$. In a representative tilted-hover trial, the robot converged to an equilibrium tilt of 52.8° (0.921 rad); the peak tilt rate and tilt acceleration during the tilt transition were 0.332 rad/s and 0.528 rad/s^2, respectively (Table I).

C. Gliding and Maneuvering

Figure 6 shows two motion primitives used in our experiments: (A) tilt regulation through differential buoyancy commands and (B) controlled descent by decreasing net buoyancy. Combining these with ascent enables thrusterless, glide-like motion; we qualitatively observed a consistent horizontal component when maintaining a nonzero tilt during ascent/descent (Fig. 2(B)).

D. Task Demonstrations

Figure 7 demonstrates a representative manipulation behavior with the gripper module attached. Starting from a grasped yellow payload at $t = 0$ s, the robot alternates between tilted ascent and tilted descent to reposition the object in the water column while maintaining a stable grasp. This example illustrates how the platform's buoyancy-driven attitude authority can be leveraged for intervention-style behaviors

Fig. 7. Thrusterless manipulation demonstration using buoyancy-driven tilt. A sequence of six snapshots (every 5 s) from $t = 0$ s to $t = 25$ s shows the gripper grasping a yellow payload and transporting it by alternating ascent and descent while regulating the vehicle tilt. The motion is achieved without thrusters by coordinating net buoyancy changes with attitude control.

without exposing propellers to entanglement risks in cluttered environments.

V. Limitations and Future Work

While the platform demonstrates repeatable volume actuation and maintains nontrivial high-angle attitudes via static buoyancy balance, several factors currently bound its performance. First, the high-level mapping from desired depth/tilt behaviors to per-engine setpoints is currently tuned empirically and may change with payload properties and environmental conditions (e.g., trapped air, water currents, and hydrodynamic interaction). Second, syringe-based mechanisms introduce non-idealities such as seal friction, backlash, and potential hysteresis, which can limit actuation bandwidth and repeatability. Third, long-term operation depends on sealing reliability and trapped-air management. Finally, wireless communication in underwater environments is challenging due to electromagnetic attenuation; the current system is most suitable for shallow-water experiments or configurations where the radio link remains viable. In our experiments, a waterproof antenna was placed near the robot in shallow water (within sub-meter range) to maintain the wireless UART link.

Despite these factors, the platform's modular magnetic interface and distributed buoyancy architecture offer a versatile foundation for diverse underwater applications. Beyond the demonstrated gripper, the system supports the rapid integration of onboard instrumentation, including cameras, lights, water-quality sensors, and task-specific end-effectors. A promising direction is *in-water payload characterization*: because buoyancy is directly controlled via displaced volume, the robot can potentially estimate the buoyant weight of a grasped object by measuring the additional volume required to maintain neutral buoyancy or a fixed depth, enabling underwater "weighing" and in-situ property estimation. Another direction is to incorporate model-based or learning-based high-level control that adapts the setpoint mapping online across payloads and hydrodynamic conditions, supporting autonomous depth/tilt regulation and more complex behaviors. With reliable state estimation and closed-loop control, the platform can be extended to trajectory tracking and path planning for efficient thrusterless glide segments and manipulation sequences. Communication can also be improved by adopting alternative links (e.g., tethered operation, optical links, or acoustic modems) and by designing protocols that tolerate packet loss and low update rates in underwater settings.

VI. Conclusion

This paper presented Manipulider, a multi-engine buoyancy-controlled underwater robot that enables thrusterless depth change, large whole-body tilting, and a magnetic modular payload interface. By modulating the center of buoyancy across four distributed engines, the robot achieves a total buoyancy authority of $\approx$160 g and maximum statically stable tilts exceeding 60°. Experimental characterization demonstrated peak vertical speeds of 95.5 mm/s and tilt rates of 0.332 rad/s, validating the robot's capacity for agile posture reconfiguration. Furthermore, we demonstrated that these motion primitives can be leveraged for thrusterless manipulation sequences, offering a low-turbulence, entanglement-resistant alternative to propeller-driven systems. Ultimately, this platform serves as a versatile foundation for future research in thrusterless underwater locomotion, autonomous multi-body manipulation, and in-situ environmental sensing in sensitive aquatic habitats.

Acknowledgment

We used LLM tools, including Codex and GPT, to assist with software implementation, writing, proofreading, and literature search. All final text and references were edited and reviewed by humans.

References

[1] S. Aracri, F. Giorgio-Serchi, G. Suaria, M. E. Sayed, M. P. Nemitz, S. Mahon, and A. A. Stokes, "Soft Robots for Ocean Exploration and Offshore Operations: A Perspective," *Soft Robotics*, vol. 8, no. 6, pp. 625–639, Dec 2021.

[2] G. Li, T.-W. Wong, B. Shih, C. Guo, L. Wang, J. Liu, T. Wang, X. Liu, J. Yan, B. Wu, F. Yu, Y. Chen, Y. Liang, Y. Xue, C. Wang, S. He, L. Wen, M. T. Tolley, A.-M. Zhang, C. Laschi, and T. Li, "Bioinspired soft robots for deep-sea exploration," *Nature Communications*, vol. 14, no. 1, p. 7097, Nov 2023.

[3] J. Qu, Y. Xu, Z. Li, Z. Yu, B. Mao, Y. Wang, Z. Wang, Q. Fan, X. Qian, M. Zhang, M. Xu, B. Liang, H. Liu, X. Wang, X. Wang, and T. Li, "Recent Advances on Underwater Soft Robots," *Advanced Intelligent Systems*, p. 2300299, Oct 2023.

[4] K. Macauley, L. Cai, P. Adamczyk, and Y. Girdhar, "Reefglider: A highly maneuverable vectored buoyancy engine based underwater robot," in *2024 IEEE International Conference on Robotics and Automation (ICRA)*. IEEE, 2024, pp. 6082–6088.

[5] K. E. Irgens, J. T. Klamo, and A. G. Pollman, "Experimental assessment of entanglement for a propeller driven unmanned underwater vehicle," *Naval Engineers Journal*, vol. 133, no. 3, pp. 103–114, 2021.

[6] B. Mitchell, E. Wilkening, and N. Mahmoudian, "Developing an underwater glider for educational purposes," in *2013 IEEE International Conference on Robotics and Automation*. Karlsruhe, Germany: IEEE, May 2013, pp. 3423–3428.

[7] A. Williams, "Design of a Low-Cost Open-Source Underwater Glider," Engineering Archive, Tech. Rep., Apr 2018, type: article.

[8] K. Bonofiglio, L. Whiteside, M. Angeles, M. Haahr, B. Simpson, J. Palmer, Y. Wu, and M. P. Nemitz, "Soft Fluidic Closed-Loop Controller for Untethered Underwater Gliders," in *2023 IEEE International Conference on Soft Robotics (RoboSoft)*. Singapore, Singapore: IEEE, Apr 2023, pp. 1–6.

[9] N. E. Leonard and J. G. Graver, "Model-based feedback control of autonomous underwater gliders," *IEEE Journal of Oceanic Engineering*, vol. 26, no. 4, pp. 633–645, 2001.

[10] J. G. Graver, "Underwater gliders: Dynamics, control and design," Ph.D. dissertation, Princeton University, 2005. [Online]. Available: https://naomi.princeton.edu/wp-content/uploads/sites/744/2021/03/jggraver-thesis-4-11-05.pdf

[11] E. Petritoli, F. Leccese, and M. Cagnetti, "Autonomous underwater glider: A comprehensive review," *Drones*, vol. 9, no. 1, p. 21, 2024.

[12] H. Wu, W. Niu, S. Wang, and S. Yan, "An optimization method for control parameters of underwater gliders considering energy consumption and motion accuracy," *Applied Mathematical Modelling*, vol. 90, pp. 1099–1119, 2021.

[13] C. C. Eriksen, T. J. Osse, R. D. Light, T. Wen, T. W. Lehman, P. L. Sabin, J. W. Ballard, and A. M. Chiodi, "Seaglider: a long-range autonomous underwater vehicle for oceanographic research," *IEEE Journal of Oceanic Engineering*, vol. 26, no. 4, pp. 424–436, 2001.

[14] J. Sherman, R. E. Davis, W. B. Owens, and J. Valdes, "The autonomous underwater glider 'spray'," *IEEE Journal of Oceanic Engineering*, vol. 26, no. 4, pp. 437–446, 2001.

[15] D. C. Webb, P. J. Simonetti, and C. P. Jones, "Slocum: an underwater glider propelled by environmental energy," *IEEE Journal of Oceanic Engineering*, vol. 26, no. 4, pp. 447–452, 2001.

[16] D. L. Rudnick, R. E. Davis, C. C. Eriksen, D. M. Fratantoni, and M. J. Perry, "Underwater gliders for ocean research," *Marine Technology Society Journal*, vol. 38, no. 2, pp. 73–84, 2004.

[17] E. Petritoli, F. Leccese, and M. Cagnetti, "High accuracy buoyancy for underwater gliders: The uncertainty in the depth control," *Sensors*, vol. 19, no. 8, p. 1831, 2019.

[18] K. Shibuya, Y. Kado, S. Honda, T. Iwamoto, and K. Tsutsumi, "Underwater robot with a buoyancy control system based on the spermaceti oil hypothesis," in *2006 IEEE/RSJ International Conference on Intelligent Robots and Systems*. Beijing, China: IEEE, Oct 2006, pp. 3012–3017.

[19] F. Fornai, G. Ferri, B. Mazzolai, and C. Laschi, "Design of a small sized self-powered robot for monitoring the ocean water column," in *2013 MTS/IEEE OCEANS - Bergen*. Bergen: IEEE, Jun 2013, pp. 1–6.

[20] C. Detweiler, S. Sosnowski, I. Vasilescu, and D. Rus, "Saving Energy with Buoyancy and Balance Control for Underwater Robots with Dynamic Payloads," in *Experimental Robotics*, B. Siciliano, O. Khatib, F. Groen, O. Khatib, V. Kumar, and G. J. Pappas, Eds. Berlin, Heidelberg: Springer Berlin Heidelberg, 2009, vol. 54, pp. 429–438, series Title: Springer Tracts in Advanced Robotics.

[21] I. Vasilescu, C. Detweiler, M. Doniec, D. Gurdan, S. Sosnowski, J. Stumpf, and D. Rus, "Amour v: A hovering energy efficient underwater robot capable of dynamic payloads," *The International Journal of Robotics Research*, vol. 29, no. 5, pp. 547–570, 2010.

[22] J. Falcão Carneiro, J. Bravo Pinto, F. Gomes de Almeida, and N. A. Cruz, "Design and experimental tests of a buoyancy change module for autonomous underwater vehicles," *Actuators*, vol. 11, no. 9, p. 254, 2022.

[23] J. Falcão Carneiro, J. B. Pinto, F. Gomes de Almeida, and N. A. Cruz, "Electrohydraulic and electromechanical buoyancy change device unified vertical motion model," in *Actuators*, vol. 12, no. 10. MDPI, 2023, p. 380.

[24] J. F. Carneiro, J. B. Pinto, F. G. de Almeida, and N. A. Cruz, "Depth control of an underwater sensor platform: Comparison between variable buoyancy and propeller actuated devices," *Sensors*, vol. 24, no. 10, p. 3050, 2024.

[25] B. K. Tiwari and R. Sharma, "Design and analysis of a variable buoyancy system for efficient hovering control of underwater vehicles with state feedback controller," *Journal of Marine Science and Engineering*, vol. 8, no. 4, p. 263, 2020.

[26] M. Elkolali, "Design and testing of a miniature variable buoyancy system for underwater vehicles," Master's thesis, Oslo Metropolitan University (OsloMet), 2022.

[27] Y. Yang, Y. Wang, Z. Ma, and S. Wang, "A thermal engine for underwater glider driven by ocean thermal energy," *Applied Thermal Engineering*, vol. 99, pp. 455–464, 2016.

[28] M. Wright, Q. Xiao, S. Dai, M. Post, H. Yue, and B. Sarkar, "Design and development of modular magnetic bio-inspired autonomous underwater robot – MMBAUV," *Ocean Engineering*, vol. 273, p. 113968, Apr 2023.

[29] S. Mintchev, R. Ranzani, F. Fabiani, and C. Stefanini, "Towards docking for small scale underwater robots," *Autonomous Robots*, vol. 38, no. 3, pp. 283–299, Mar 2015.

[30] J. Liu, S. Iacoponi, C. Laschi, L. Wen, and M. Calisti, "Underwater Mobile Manipulation: A Soft Arm on a Benthic Legged Robot," *IEEE Robotics & Automation Magazine*, vol. 27, no. 4, pp. 12–26, Dec 2020.

[31] M. Wu, X. Zheng, R. Liu, N. Hou, W. H. Afridi, R. H. Afridi, X. Guo, J. Wu, C. Wang, and G. Xie, "Glowing Sucker Octopus (*Stauroteuthis syrtensis*)-Inspired Soft Robotic Gripper for Underwater Self-Adaptive Grasping and Sensing," *Advanced Science*, vol. 9, no. 17, p. 2104382, Jun 2022.

[32] E. Morgan, I. Carlucho, W. Ard, and C. Barbalata, "Autonomous underwater manipulation: Current trends in dynamics, control, planning, perception, and future directions," *Current Robotics Reports*, vol. 3, no. 4, pp. 187–198, 2022.

[33] S. Lensgraf, A. Sniffen, Z. Zitzewitz, E. Honnold, J. Jain, W. Wang, A. Li, and D. Balkcom, "Droplet: Towards autonomous underwater assembly of modular structures," in *Proceedings of Robotics: Science and Systems*, 2021.

[34] G. Marani, S. K. Choi, and J. Yuh, "Underwater autonomous manipulation for intervention missions auvs," *Ocean Engineering*, vol. 36, no. 1, pp. 15–23, 2009.